# Experiments on the low-frequency oscillation of a separated shear layer

S. Mohamed Aniffa and Alakesh Ch. Mandal
*Department of Aerospace Engineering, Indian Institute of Technology, Kanpur 208016, India*

(Received 6 March 2022; accepted 18 January 2023; published 13 February 2023)

An experimental investigation has been carried out to study the effect of the low-frequency oscillation of a separated shear layer. A separated shear layer was generated on a flat plate placed horizontally in a low-speed wind tunnel using a contoured wall at the top of the tunnel test section. Two different contoured walls were used to impose a low and high level of adverse pressure gradient in the flow. The time-resolved particle image velocimetry measurements were carried out to study the unsteady characteristics of the separated shear layer. The measured data reveals that the vortex shedding associated with the separating shear layer is regular for the low adverse pressure gradient case, whereas it is found to be irregular or intermittent for the high adverse pressure gradient. We find that the intermittent nature of the vortex shedding for the high adverse pressure gradient case is due to a low-frequency oscillation of the shear layer and the associated movement of the points of inflection in the velocity profiles. The short time-averaged velocity profiles in the intermittent vortex-shedding process are also found to follow the embedded shear layer scaling proposed by Schatzman and Thomas [J. Fluid Mech. **815**, 592 (2017)]. We study the effect of this low-frequency oscillation on the stability characteristics of the separated shear layer and the vortex-shedding process. Based on the analyses, a nondimensional parameter ($\delta^*_{\rm rms}/\delta^*$) is proposed to quantify the interaction level of the low-frequency oscillation on the vortex shedding. We find that the interaction of the low-frequency oscillation on the vortex shedding vanishes as $\delta^*_{\rm rms}/\delta \rightarrow 0$. Further, it shows that when the numerical value of this parameter approaches 0.23, the interaction is found to be intensified, leading to the separated shear layer either from a non-vortex-shedding state to vortex-shedding state or a vortex-shedding state to a non-vortex-shedding state.

DOI: 10.1103/PhysRevFluids.8.023902

## I. INTRODUCTION

Flow separation is often encountered in various practical applications, for example, in an aircraft wing, wind turbine blades, gas turbine blades, surface of a ship, roof of a car, train, and other automobiles, etc. [1–5]. It adversely affects the aerodynamic performance of a body. Several studies were carried out to understand the flow separation and its effect on aerodynamic forces and moments. Typically, the flow separation is classified as geometry-induced or pressure-induced separation [6]. When a flow is subjected to a severe adverse pressure gradient, it separates from the surface. This separation is termed as pressure-induced separation. The former occurs when the flow passes over a sharp corner [6]. These separated shear layers may or may not reattach with the wall, as reattachment depends on the flow parameters such as velocity and pressure gradient. However, while the separated shear layer reattaches with the wall, it forms an enclosed region called a separation bubble. Under some circumstances, the separated shear layer may not reattach with the wall, for example, during an aerodynamic stall. In both cases, the transition mechanism in the separated shear layer needs to be adequately understood for effective control of the flow separation or its adverse effect [7].

 

When a shear layer separates from a surface, the velocity profiles in the separated region become inflectional, leading to amplification of the disturbances [8]. Eventually, the flow becomes unstable and forms a two-dimensional (2D) roller/vortex structure. This inflectional instability, called Kelvin-Helmholtz (KH) instability, is commonly accepted as the primary instability mechanism in the separated shear layer [8–11]. An instability that develops in a 2D roller or vortex is called secondary instability [11,12]. The secondary instability may be an elliptical instability (in the vortex core) or a hyperbolic instability (in the braid region of a 2D roller) [11]. These secondary instabilities are responsible for faster disintegration or breakup of the 2D rollers, leading the flow to a turbulent reattachment with the wall. In the context of frequency or modes, two different types of modes are observed in the separated shear layer: the high-frequency and the low-frequency modes. It is commonly accepted that vortex shedding causes the high-frequency mode. However, several reasons have been given for the low-frequency modes in the separated shear layer.

The low-frequency modes are often associated with bubble bursting [13–21]. Bubble bursting is the process of a sudden change in length and height of a separation bubble [13–27]. Under normal circumstances (i.e., at a low level of free stream turbulence), a separated shear layer reattaches with the wall and forms a short bubble. When the velocity decreases below a certain value, or while the angle of incidence of a body increases beyond a certain value, the length and height of the resulting separation bubble increase suddenly and form a long bubble over the body. This process is called bubble bursting. Bubble bursting is found to be the primary reason for the stall of an aerofoil [28].

Therefore, several studies were performed on aerofoils near the stall angle of attack to investigate the bubble bursting phenomenon [13–21]. The instantaneous lift coefficient ($C_L$) shows a quasiperiodic or periodic oscillation with time [13]. It appears that this low-frequency oscillation is due to the periodic switching between a short and a long bubble near the stall angle of attack (AOA). Almutairi and AlQadi [13] carried out phase averaging based on the $C_L$ variation (oscillation cycle) to find different behaviors of the bubble at an AOA at which the low-frequency oscillation occurs. Short bubble forms while the $C_L$ value reaches its maximum in their periodic cycle. On the other hand, the flow completely separates when the $C_L$ value reaches its minimum value in their periodic cycle. The phases in between $C_{L,\max}$ and $C_{L,\min}$, show the growth or decay of a separation bubble over an aerofoil. The amplitude of the low-frequency oscillation (i.e., amplitude of $C_L$) is also found to increase with AOA and Reynolds number [29]. The maximum reverse flow intensity in terms of local free stream velocity or the boundary layer edge velocity ($U_e$) is reported to be greater than 20% in the case of a bubble bursting [13,18,21]. This value is greater than the critical value (15–20 %) for the absolute instability in a separated shear layer [30]. Hence, it was speculated that absolute instability could be one of the reasons for bubble bursting.

Using spectral analysis, Almutairi *et al.* [18] hypothesized that the low-frequency oscillation is due to the formation of a low-pressure region resulting from the large-scale vortex shedding near the trailing edge. They carried out the dynamic mode decomposition (DMD) analysis to support this hypothesis. In some studies, instead of investigating the aerofoil at some particular AOA (near stall), the aerofoil was smoothly pitched up to produce a bubble bursting process [19]. The temporal evolution of the bubble was monitored using the skin-friction coefficient ($C_f$) and the instantaneous displacement thickness ($\delta_I^*$). The reattachment point was found to move in the downstream direction with time. The velocity of the reattachment point for the case of a long bubble (17% $U_e$) was reported to be one order greater than that for the short bubble (1.7% $U_e$). Furthermore, the numerical value of the reverse flow intensity also exceeded the critical value for the absolute instability, even for the short bubble case. They observed the rapid increase in shear layer height in the wall-normal direction in the process of a long bubble formation. Hence, they concluded that bubble bursting is not mainly due to the change in the type of instability (from convective to absolute), but it is due to a change in the stability characteristics (due to the increase in the shear layer height from the wall) of the separated shear layer. The recent study of Eljack *et al.* [21] shows the amplitude of the low-frequency oscillation increases beyond the stall angle of an aerofoil due to the switching between a short and a long bubble. However, this amplitude was found to decrease with a further increase of angle of attack. They concluded that the decrease in the amplitude of low-frequency oscillation is due to merging the leading edge and trailing edge separation bubbles.

As reported in various studies on flow over an airfoil, the low-frequency unsteadiness was also observed in a separated shear layer induced by a blunt leading edge [31–33]. The power spectral and correlation analyses of the pressure data reveal low- and high-frequency oscillations in these geometry-induced separation bubbles [31]. The low-frequency oscillation is attributed to the flapping of the shear layer, whereas the high-frequency oscillation is due to regular vortex shedding. Moreover, it was conjectured that while the vorticity accumulation exceeds a certain value, the large-scale vortex sheds downstream. Consequently, the shear layer moves inward/towards the wall. Similarly, the shear layer moves outward/towards the free stream when vorticity accumulation occurs. These inward and outward motions of a separated shear layer that contribute to shrinkage and enlargement of a bubble, respectively, are responsible for low-frequency oscillation. The existence of such low-frequency oscillation was also confirmed in some subsequent studies [32,34,35]. In contrast, some authors reported that the low-frequency oscillation is absent (based on the power spectra of the pressure signal), and only high-frequency vortex shedding is present [36,37].

The separated flow in a backward-facing step is also found to be associated with both the low- and high-frequency oscillations [38]. While the high frequency is associated with the shear layer shedding [38], the low-frequency flapping motion is due to "instantaneous imbalance between the entrainment rate from the recirculation zone and the reinjection rate near reattachment," as reported by Eaton and Johnston [39]. However, Spazzini *et al.* [40] conjectured that the low-frequency flapping motion is due to oscillatory behavior of the secondary recirculation region in backward-facing step.

These studies, as reviewed above, sufficiently establish the fact that both low- and high-frequency modes are involved in the instability process of a separated shear layer. However, the effect of the former on the vortex-shedding process is not well understood. Therefore, the present experimental investigation aims to find the effect of a low-frequency oscillation on the high-frequency vortex shedding. Moreover, an attempt is made to find a parameter that quantifies the interaction level of a low-frequency oscillation on a high-frequency vortex shedding. This paper is organized as follows. The detailed experimental setup is given in Sec. II, followed by the results and discussion in Sec. III. The conclusions drawn from the analyses are presented in Sec. IV.

## II. EXPERIMENTAL SETUP

The present experimental work was carried out in a low-speed, open circuit wind tunnel. It is a suction-type tunnel. The honeycomb section houses six screens to enhance the flow quality in the test section. It has a square test section of 610 mm$\times$ 610 mm, and its length was 3000 mm. The test section was followed by a diffuser. A fan at the end of the diffuser is driven by a 15 HP motor, which is controlled by a speed controller (made by Siemens). This tunnel was used in many previous experimental studies [41,42].

A contoured wall, made of wood, is often placed over the upper surface of the test section to impose the adverse pressure gradient (APG) over a flat plate, e.g., [9,43]. Here, two different levels of adverse pressure gradients were imposed by using different wall angle ($\theta$), as shown in Fig. 1. The contoured wall consists of three parts, namely, accelerating, stabilizing, and decelerating parts. The lengths of accelerating and stabilizing parts are 400 mm and 100 mm, respectively. The maximum depth of the stabilizing part is 165 mm. By changing the wall angle of the decelerating part ($\theta = 7.5^\circ$ and $15^\circ$), different levels of adverse pressure gradients were imposed, as schematically shown in Figs. 1(a) and 1(b). In the following, we refer to the measurements associated with the first setup [Fig. 1(a)] with an angle of $7.5^\circ$ as case 1 (low adverse pressure gradient case), and with the second one [Fig. 1(b)] with an angle of $15^\circ$ as case 2 (high adverse pressure gradient case). A slot of 10 mm wide at the center of the top surface of the contoured wall was made to pass the laser sheet for the particle image velocimetry measurements (PIV) in the wall-normal plane ($x$-$y$ plane). The flow was tripped using a circular tripping device of 10 mm diameter, placed at the middle of the

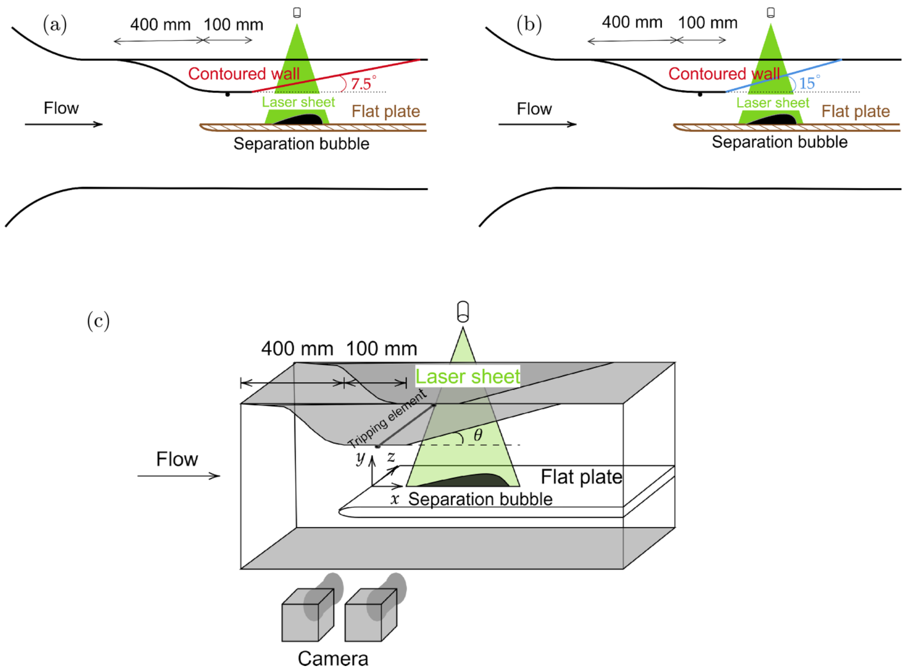


FIG. 1. A simple schematic for the experimental setup used in the present work. (a) Side view of the experimental setup for imposing low level of adverse pressure gradient. (b) Side view of the experimental setup for imposing high level of adverse pressure gradient. (c) Isometric view of the experimental setup.

stabilizing part to prevent the flow separation in the diverging section of the contoured wall. Using PIV measurements on a plane normal to the surface of the contoured wall, we have ensured that there is no flow separation along the diverging portion of the test section.

The flat plate was made up of an acrylic sheet of 12 mm thickness; its length and width are 1200 mm, and 609 mm, respectively. It has a an asymmetric modified superelliptic leading edge, as detailed in Balamurugan and Mandal [41]. The leading edge profile considered has been shown to reduce the pressure gradient along its surface [41,44,45]. The separation bubbles were generated over this flat plate, which was placed horizontally at the center-line of the test section of the tunnel.

A time-resolved particle image velocimetry (TR-PIV) technique was used for all the measurements reported in this paper. The TR-PIV system consists of a high-frequency double pulsed Nd: YLF laser (Photonics Industries, dual head DPSS, energy 30 mJ per pulse at 527 nm at the repetition rate of 1 kHz), a COMS camera and a synchronizer (IDTvision, USA). The arrangements for the TR-PIV measurements in the wall-normal plane are schematically shown in Fig. 1(c). We used two different CMOS cameras: CMOS-1 camera (Y5, IDTvision, USA, resolution, 2560 $\times$ 1920 pixels, 4MP, with the maximum frame rate at maximum resolution is 365 Hz at double exposure mode) and CMOS-2 camera (Os 10-4K camera, IDTvision, USA, resolution, 3840 $\times$ 2400 pixels, 9 MP, with the maximum frame rate at maximum resolution is 500 Hz at double exposure mode). The flow was seeded with fog particles of mean diameter of about 1 $\mu m$ using a fog generator (SAFEX fog generator, Dantec Dynamics, Denmark). The laser and the camera were synchronized using the MotionPro timing unit (IDTvision, USA) and the TSI synchronizer (TSI, USA). Two CMOS-1 cameras were placed side by side [Fig. 1(c)] and used simultaneously to measure the mean flow characteristics over a field of view of 300 mm$\times$ 84 mm, whereas only CMOS-2 camera was utilized to measure the unsteady flow characteristics over a field of view of 154 mm $\times$ 87 mm. A total of 1050 image pairs were acquired at three different sampling frequencies, i.e., 30 Hz, 100 Hz, and 200 Hz. A total of 3150 image pairs were considered for the mean flow characteristics. On the

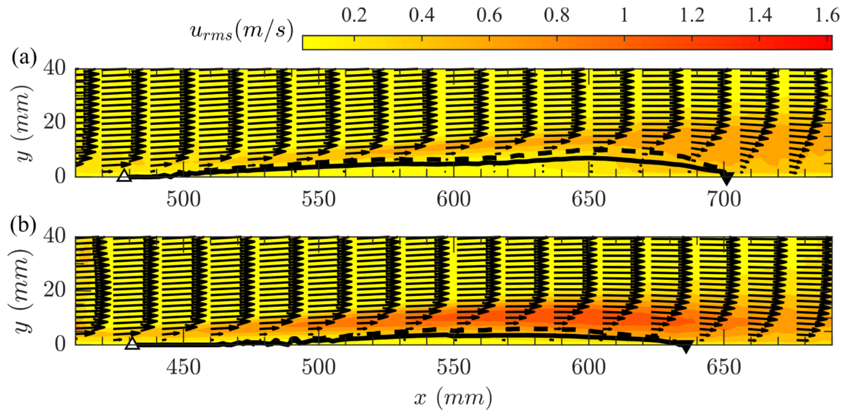


FIG. 2. Mean flow velocity vectors superimposed with $u_{\rm rms}$ contour. (a) Case 1 (low adverse pressure gradient case). (b) Case 2 (high adverse pressure gradient case). $\triangle$: point of separation; $\blacktriangledown$: point of reattachment; _ _ _: $U = 0$ line; ___: mean dividing stream line.

other hand, a total of 1400 image pairs were acquired at a rate of 200 Hz for the unsteady flow characteristics investigation. All the acquired images were processed using the mess-free software, ProVision-XS (IDTpiv), with a correlation window of 32 pixels $\times$ 32 pixels and then instantaneous velocity vector fields were obtained. The maximum uncertainty of the measured velocity is found to be approximately 3.39% of the free stream velocity. The uncertainty analysis was carried out following the literature [41,42,46–49]. This PIV system and the processing package was used in our various previous works [41,50].

A hot-wire anemometry system, which was procured from DANTEC Dynamics, Denmark, was also utilized in the present study. A single wire probe (55P11, Dantec Dynamics), which has a sensing element made of tungsten wire of 5$\mu$m diameter, was used for data acquisition. The length-to-diameter ratio of the sensing element is 250. The hot-wire probe was calibrated using the PIV measurements and the King's law fit. The data were acquired at a rate of 2 kHz using a 16-bit data acquisition card and LABVIEW software.

In the present study, the streamwise and wall-normal directions are represented by $x$ and $y$, respectively, with the origin located at the leading edge of the flat plate. The reference velocity $U_r = 2$ m/s, which was measured at 650 mm ahead of the leading edge. We may note that the reference velocity was measured well ahead of the contoured wall section.

## III. RESULTS AND DISCUSSIONS

The results obtained from the high-resolution TR-PIV measurements are presented below. In the following, the measurements for the low and high adverse pressure gradient cases referred as case 1 and case 2, respectively, as mentioned above. Furthermore, red and blue lines or symbols in all the figures below represent case 1 and case 2, respectively, in the entire paper. Time, $t$, is in seconds (s), and $\Delta t$ refers to time separation between two consecutive TR-PIV realizations. We may also mention that $t = 0$ s refers to the first TR-PIV realization.

### A. Mean flow characteristics

Figure 2 shows the measured mean flow velocity vectors overlaid with the contours of $u_{\rm rms}$; here $u_{\rm rms}$ denotes the root mean squared value of the streamwise fluctuating velocity, $u$. The separation bubble can be identified either by the isoline of zero streamwise mean velocity, $U = 0$, or by the mean dividing streamline, $y_d$; it is the wall-normal height at which the integration of $U$ becomes zero [51]. The points of separation and reattachment, which are identified following the procedure

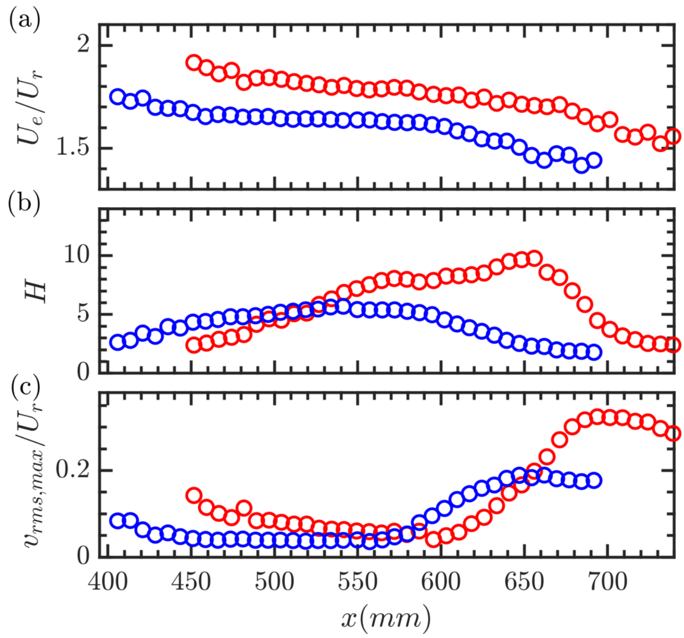


FIG. 3. Comparison of the mean flow parameters between case 1 and case 2. (a) Boundary layer edge velocity. (b) Shape factor. (c) Root mean squared value of wall-normal fluctuating velocity. Description of symbols: (○) case 1, (○) case 2.

mentioned in Ref. [52], are denoted by $x_s$ and $x_r$, respectively. However, one may notice in Fig. 2 that an increase in pressure gradient (case 2) leads to earlier separation and reattachment, as compared to the lower pressure gradient (case 1). The maximum height of the bubble is also found to decrease for the case 2. The pressure gradient parameter, $P(=\frac{y_{d,\max}^2}{\nu}\frac{\Delta U}{\Delta X})$, is also estimated to determine whether the bubble is a short bubble or a long bubble; here $y_{d,\max}$ denotes the maximum height of the mean dividing streamline from the wall, and $\Delta U$ and $\Delta X$, denote the difference in the mean velocity and spatial distance $(x_r - x_s)$ between the points of separation and reattachment. The value of $P$ for case 1 and case 2 is found to be $-3.4$ and $-1.7$, respectively. These values are greater than the threshold value mentioned in Ref. [24] for the formation of a long bubble, i.e., $P > -28$. The Reynolds numbers at the point of separation ($\mathrm{Re}_{\delta^*,s} = U_e\delta^*/\nu$) are found to be 942 and 796, for case 1 and case 2, respectively; here, $U_e$ and $\delta^*$ represent the boundary layer edge velocity (the maximum streamwise mean velocity at a $x$ location) and the displacement thickness at the point of separation, respectively. The value of $\mathrm{Re}_{\delta^*,s}$ should be less than 400 for the formation of a long bubble [23]. Therefore, based on both of the parameters, i.e., $P$ and $\mathrm{Re}_{\delta^*,s}$, the present separation bubbles for both the cases considered are found to be short separation bubbles. Figure 3(a) shows the variation of the boundary layer edge velocity, $U_e$; here, the reference velocity, $U_r$, as mentioned in the previous section, is used for normalization. This variation serves as a boundary condition for the separated flow, similar to the one reported in the literature [53–55]. Moreover, one may note that the boundary layer edge velocity variation can compare with the pressure variation in the separated flow studies [55]. Figure 3(b) shows the variation of the shape factor ($H$). The shape factor is the ratio of displacement thickness ($\delta^*$) to the momentum thickness ($\theta$). The shape factor reaches its maximum value, followed by a rapid decrease, implying that the transition takes place in the measurement region [56,57]. The variation of $v_{\mathrm{rms,max}}$ is shown in Fig. 3(c); here, $v_{\mathrm{rms}}$ represents the root mean squared value of the wall-normal fluctuating velocity. Increasing $v_{\mathrm{rms,max}}$ in the streamwise direction indicates that the shear layer roll up takes place in the separated shear layer [58]. It also shows that

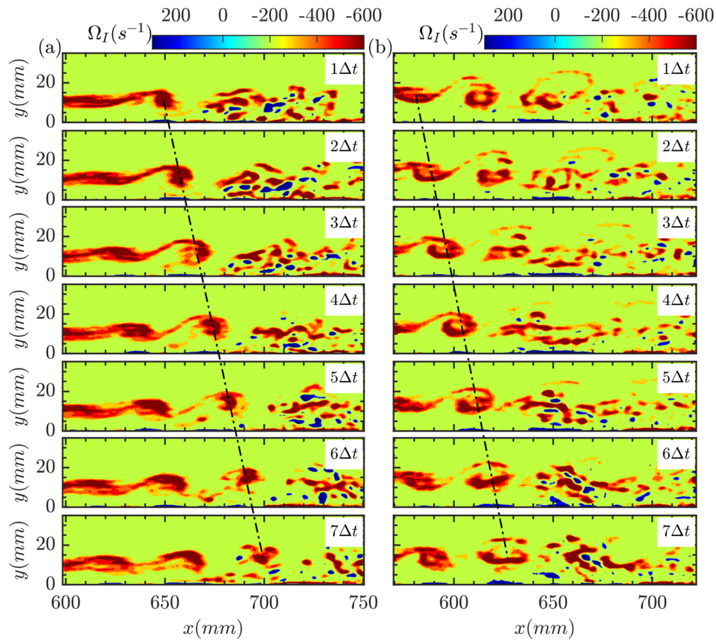


FIG. 4. Time sequence of the vortex-shedding structure showing its evolution and propagation. (a) Case 1 (low adverse pressure gradient case). (b) Case 2 (high adverse pressure gradient case).

the disturbances initially get amplified in the downstream direction, followed by a maximum value within the measurement region. This is attributed to the transition and onset of turbulence in the separated shear layer [58]. Further, an early maximum value of $v_{\mathrm{rms}}$ for the high-pressure gradient case is seen, as compared to the low-pressure gradient case. On the whole, these mean flow results confirm that the measurement region can capture the unsteady characteristics of the separated shear layer for both the cases studied here.

### B. Unsteady flow characteristics

The time sequences of the instantaneous vorticity fields of the separated shear layers are shown in Figs. 4(a) and 4(b), for case 1 and case 2, respectively. These figures clearly show the presence of the vortex shedding for both cases, as expected. However, careful examination of the entire time sequence of the vorticity contours reveals that the vortex shedding is intermittent for case 2, whereas it is found to be regular for case 1. Three phases in the vortex-shedding dynamics are identified for case 2, called here as stable phase, shedding phase with upstream propagation of the entire vortex shedding region, and shedding phase with downstream propagation of the entire vortex-shedding region, as shown in Figs. 5(a)–5(c), respectively. Occurrences of these events are found to be associated with low frequency, which is the main focus of the present study. For detailed discussions about these low-frequency dynamics, instantaneous TR-PIV realizations at some regular time intervals are shown in Figs. 6(a) and 6(b), for case 1 and case 2, respectively. The vortex shedding can be seen to be present in all the panels in Fig. 6(a), for case 1, indicating the presence of nearly regular shedding. In contrast, Fig. 6(b) clearly shows the presence of intermittent/irregular shedding, for case 2. In Fig. 6(b) at $t = 1$ s, the concentrated vorticity region shows no sign of vortex shedding. As time progresses, the separated shear layer is seen to oscillate and rolls up to form a vortex structure at $x = 650$ mm (see the panel at $t = 2$ s). The oscillation in the shear layer is also seen to propagate upstream direction leading to the formation of an early vortex structure (see the panel at $t = 3$ s), and at later time, it is seen to shift in the downstream direction

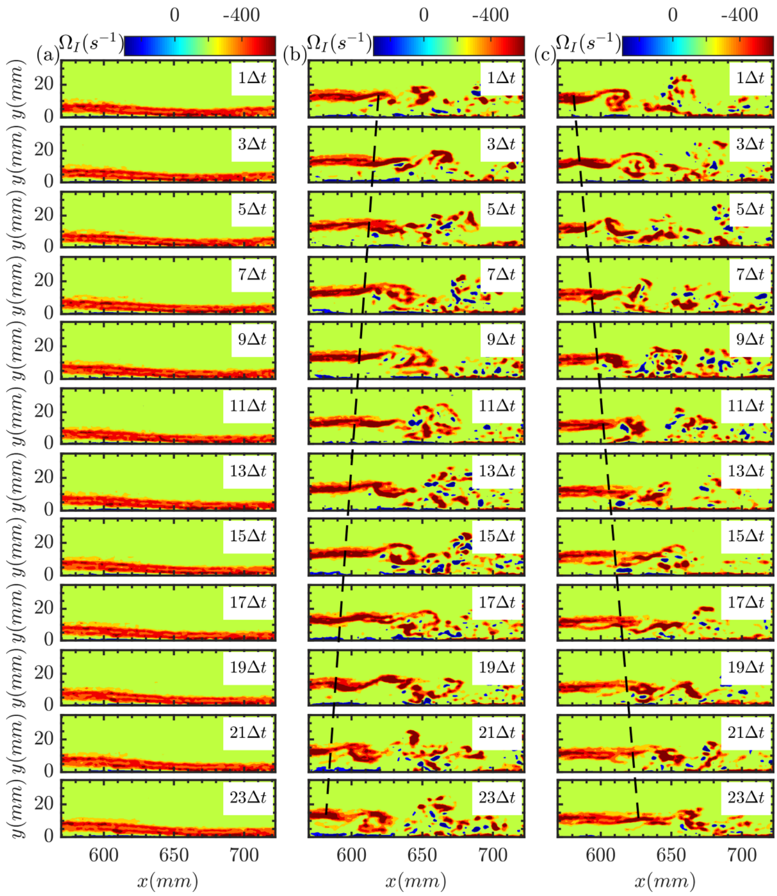


FIG. 5. Time sequence of instantaneous vorticity contours at three different phases for case 2. (a) Stable phase. (b) Shedding phase with upstream propagation of the entire vortex-shedding region. (c) Shedding phase with downstream propagation of the entire vortex-shedding region. The onset of the oscillation is indicated by a dashed line in (b) and (c).

(see the panel at $t = 4$ s). Eventually, as time progresses further, the vortex structure is found to be absent, and the concentrated vorticity region again shows no sign of vortex shedding in the entire measurement region as found at $t = 1$ s. This intermittent shedding/cyclic instability of the separated shear layer, as obtained from the time sequences of the TR-PIV measurements, has not been reported in the literature, to the best of our knowledge. However, the intermittent short pulse signal in the hot-wire signal was reported in the study of bubble bursting [22], which might be due to the intermittent shedding of the separated shear layer. The presence of bubble bursting is often attributed to the absolute instability of the separated shear layer [12,18,29], which is seen to occur at the maximum reverse flow intensity ($\frac{U_{\min}}{U_e}$) of around 15% [30]. For the present case, The maximum reverse flow intensities were found to be 0.93% and 7.32%, for case 1 and case 2, respectively. Therefore, as far as the reverse flow is concerned, the present intermittent characteristics cannot be attributed to the presence of bubble bursting. For further understanding of this phenomenon, the instantaneous displacement thickness [19] is estimated from the instantaneous velocity fields, as this quantity is useful in characterizing the shear layer height from the wall. The instantaneous displacement thickness, $\delta_I^*$, was estimated from the instantaneous velocity profile extracted at a location close to the onset of $v_{\text{rms,max}}$ growth, as shown in Fig. 3(c). To be specific, it was estimated

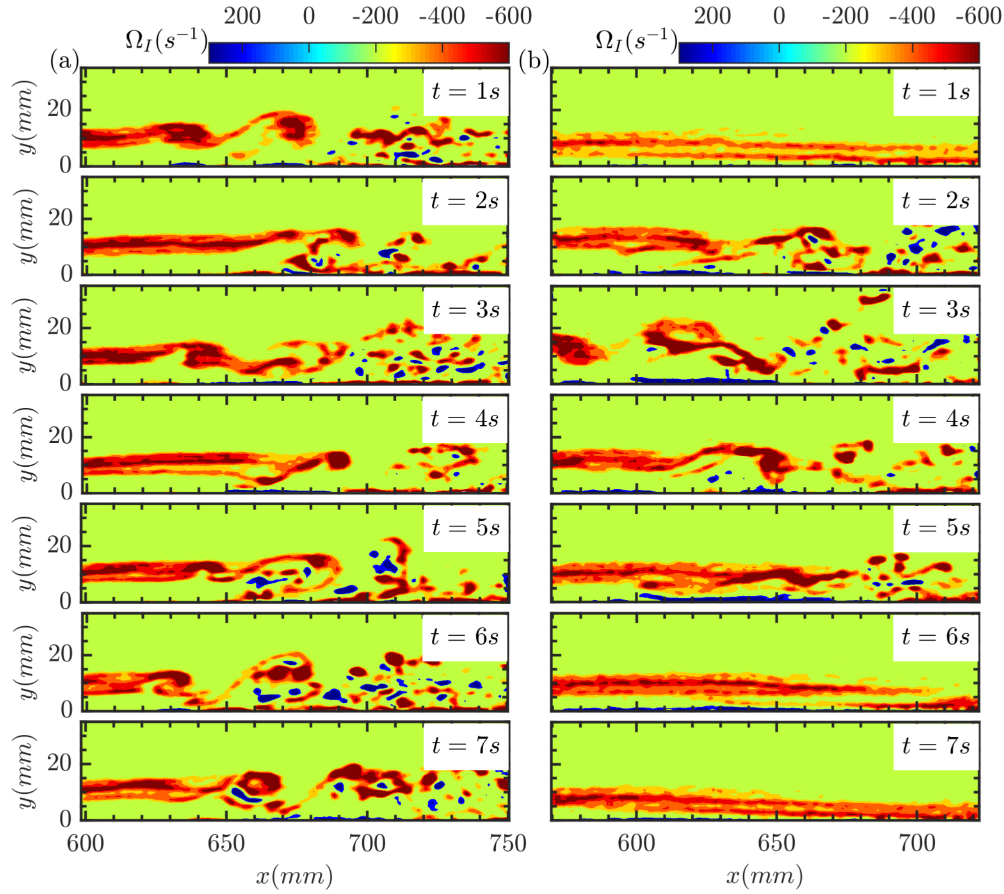


FIG. 6. Instantaneous vorticity contours at a regular long time interval. (a) Case 1 (low adverse pressure gradient case). (b) Case 2 (high adverse pressure gradient case).

at $x = 624$ mm, for case 1, and at $x = 596$ mm, for case 2. The time series of $\delta_I^*$ is shown in Fig. 7, for both the cases. We may note that a similar variation was also observed for the Reynolds number, $\mathrm{Re}_{\delta_I^*}(= U_{e,I}\delta_I^*/\nu)$, defined based on the instantaneous displacement thickness and the instantaneous boundary layer edge velocity ($U_{e,I}$). However, $\mathrm{Re}_{\delta_I^*}$ is found to vary within $1961 \leqslant \mathrm{Re}_{\delta_I^*} \leqslant 3069$ and $1213 \leqslant \mathrm{Re}_{\delta_I^*} \leqslant 4106$, for the case 1 and case 2, respectively. A similar range of values has also been reported for other separated flows in the literature [59]. The red and blue dashed lines in Fig. 7 indicate the mean values of the displacement thicknesses, obtained from the mean velocity profiles. A very high oscillation with respect to the mean displacement thickness can be noticed for case 2, as compared to the low oscillation for case 1. This oscillation of the time series about the mean can be attributed to the movement of the shear layer from the wall, as detailed below.

Various time instants corresponding to the panels shown in Fig. 6 are also marked in Fig. 7. Comparing these two figures, one can see that there is no vortex formation when $\delta_I^*$ is at its lower value. This can be due to the viscous effect, which dampens the instability process and suppresses the vortex formation in the separated shear layer. However, as time progresses, the shear layer is seen to move away from the surface and reaches its maximum position at $t \approx 2.2$ s (see Fig. 7). When the shear layer moves away from the wall, it becomes more prone to inflectional instability. Consequently, the high-frequency oscillation can be seen in $\delta_I^*$ within the time interval of $t \approx 2.2$–4 s, as compared to other time intervals in Fig. 7. It is due to the vortex shedding which

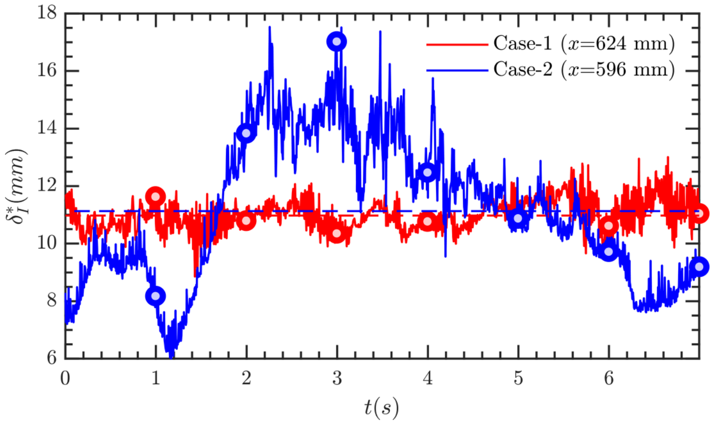


FIG. 7. Comparison of the instantaneous displacement thickness between case 1 and case 2. Red (— —) and blue (— —) dashed lines represent the mean displacement thickness for case 1 and case 2. The red and blue circles indicate the time instants corresponding to those shown in various panels of Fig. 6.

can be seen from the instantaneous vorticity contour [see Fig. 6(b) at $t = 3$ s]. During the shedding process, the shear layer gradually moves towards the wall, as seen from Figs. 6 and 7, resulting in velocity profiles, which are less prone to inflectional instability. When the displacement thickness value decreases to its lower level at $t = 7$ s, the vortex shedding is completely suppressed, as seen in Fig. 6(b) at $t = 7$ s. Figure 7 also shows that the shear layer moves away from the surface rapidly ($t \approx 1$ s$-2$ s), as compared to its movement towards the wall ($t \approx 2.2$ s$-6$ s).

The unsteady characteristics of the separated shear layer can also be characterized by the streamwise ($u$) and wall-normal ($v$) fluctuating velocity components. The time-series signals of the streamwise and wall-normal fluctuating velocity components extracted at $y = \delta^*$ are shown in Figs. 8(a) and 8(b), for case 1 and case 2, respectively. It may be noted that it is a common practice [59–61] to extract time-series signal at $y = \delta^*$ in a separated flow. Since the transition location is seen to change with space and time, the time-series signals are shown at different streamwise locations. Figure 8(a) shows that the low-frequency oscillation is not prominent for case 1, as compared to the $u$ fluctuating velocity signal in Fig. 8 for case 2. That is, for the high adverse pressure gradient, the low-frequency oscillation is very clear in $u$ fluctuating velocity signal. Similar low-frequency oscillation in the $u$ fluctuating signal has already been reported in the long bubble cases [22,62]. However, these authors did not study the flow structures related to this low-frequency oscillation. Moreover, the intermittent fluctuation, similar to those seen in Fig. 8(b), was interpreted as a turbulent spot by Anand and Sarkar [62]. Figure 8(b) also shows that a high-frequency fluctuation starts while the $u$ fluctuation reaches minimum value, and this fluctuation again disappear while the $u$ fluctuation increases from negative to positive values. Comparing this fluctuating signal with the instantaneous $\delta^*$ in Fig. 7, one can find that the fluctuating velocity signal is strongly related to the shear layer movement. In other words, $u$ fluctuation reaches its minimum value when $\delta^*$ reaches its maximum value, and vice versa. Hence, it can be interpreted that when the shear layer moves sufficiently away from the wall, vortex shedding occurs, and it gradually dies when the shear layer moves towards the wall. This movement of the shear layer causes the low-frequency oscillation, and the vortex shedding causes the high-frequency oscillation. Interestingly, the $v$ fluctuating signal is not affected by the low-frequency oscillation. It only shows high amplitude fluctuation when vortex shedding is present. Further, the fluctuating duration increases with streamwise distance, as seen for case 2; a similar observation is reported in the literature [22]. Here, it is due to the shift in the transition point of the separated shear layer with time, which was discussed earlier. Hence, the striking point here is that the transition point changes with time due to the change of stability characteristics of the separated shear layer.

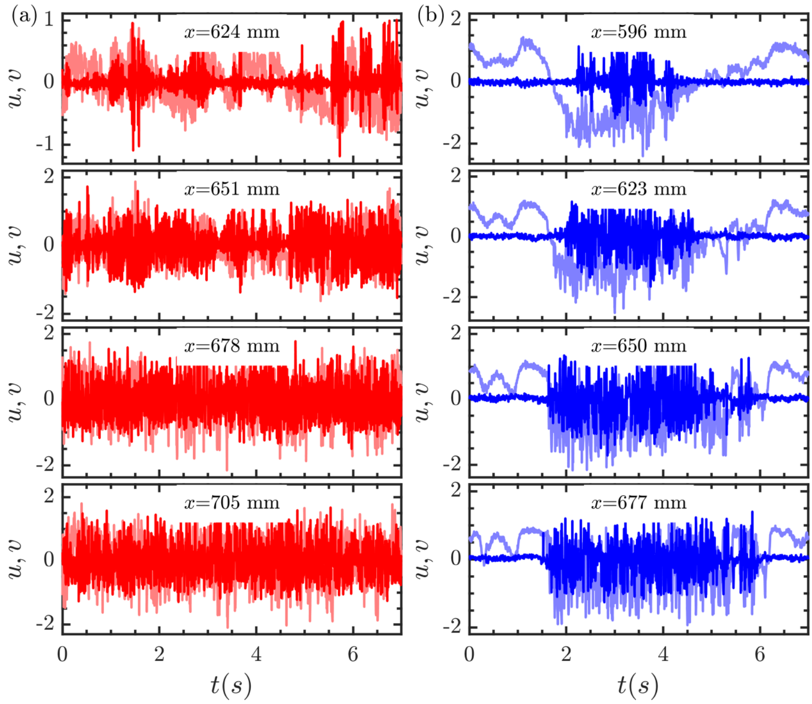


FIG. 8. The time series signal of streamwise and wall-normal fluctuating velocity components extracted at $y = \delta^*$. (a) Signals for case 1 (low adverse pressure gradient case) [—— u (in m/s), —— v (in m/s)]. (b) Signals for case 2 (high adverse pressure gradient case) [—— u (in m/s), —— v (in m/s)].

The recent experimental study on an attached turbulent boundary layer subjected to an adverse pressure gradient shows the possibility of embedded shear layer instability [1]. To investigate the embedded shear layer instability in the present study, the instantaneous velocity profiles are considered at $x = 624$ mm and $x = 596$ mm, for case 1 and case 2, respectively. The instantaneous velocity profiles are short-time averaged in the interval of $t - 5\Delta t < t < t + 5\Delta t$. The short-time averaged velocity profiles at different time instants are shown in Fig. 9. The experimentally measured velocity profiles are curve fitted following [63] to calculate the derivative $(dU/dy)$ of the velocity profiles and their inflection points $(y_{in})$. The derivative of the velocity profiles and the inflection points are also shown in Fig. 9. One may clearly notice that height of the point inflection from the wall is nearly the same at different time instants, for case 1, whereas it significantly changes with time, for case 2. The shape of the velocity profile also changes at different time instants, for case 2. All the velocity profiles in Fig. 9 are normalized using the embedded shear layer scaling, that is, $U^* = \frac{U_e - U}{U_e - U_{in}}$ and $\eta = \frac{y - y_{in}}{\delta_w}$, respectively [1], where the vorticity thickness, $\delta_w = \frac{U_e - U_{in}}{(\frac{dU}{dy})_{\max}}$, and are shown in Figs. 10(a) and 10(b), for cases 1 and 2, respectively. This figure shows a better collapse of the velocity profiles in the embedded shear layer scaling for both the cases. Further, the present data also compare well with the analytical equation, $U^* = 1 - \tanh(\eta)$, for the embedded shear layer scaling for $\eta > -1.5$. The deviation for $\eta < -1.5$ from the analytical profile can be attributed to the no-slip boundary condition of the flow at the wall. Such similar deviation is also reported and discussed in detail in Ref. [1]. The present investigation thus reveals the presence of an embedded shear layer instability in both the stable and shedding phases, for case 2. In other words, the time-dependent instability occurs via the inflectional velocity profiles.

To find out the frequency characteristics of the shed vortices, spectral analysis was carried out for the time-series signals shown in Fig. 8, and the results are presented in Fig. 11. The power

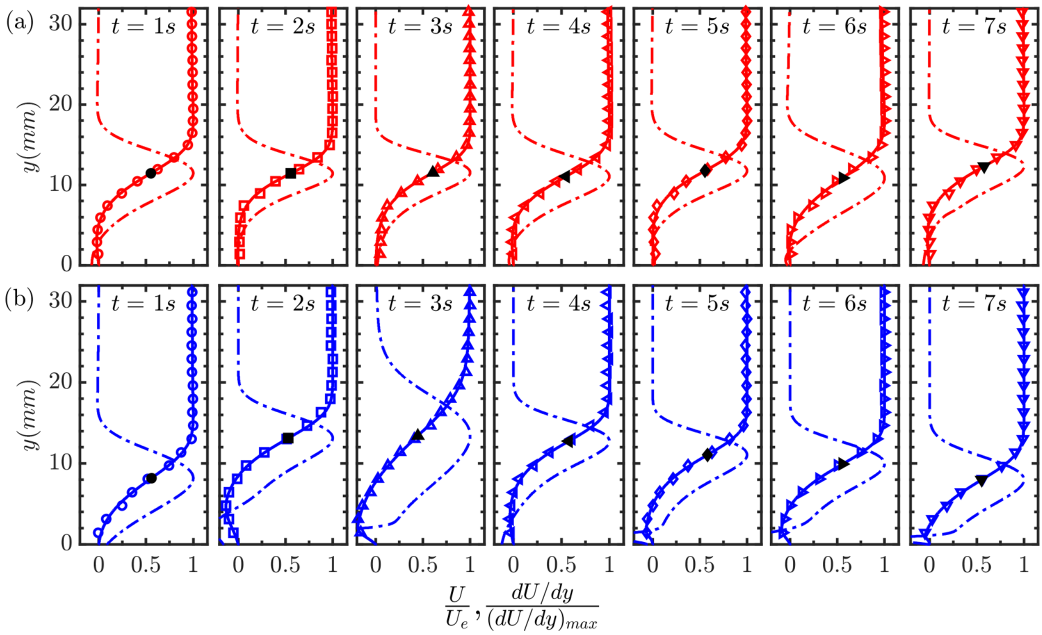


FIG. 9. Variation of the instantaneous velocity profiles at $x = 624$ mm and $x = 596$ mm for the case 1 and case 2, respectively. Symbols for measured streamwise velocity: solid lines, curve-fitted velocity profiles; dashed lines, $dU/dy$; solid symbols, inflection points of the velocity profiles.

spectrum of $u$ fluctuating component shows that the maximum power occurs at a lower frequency for both the cases, but the power spectrum of $v$ component shows a clear peak at around 50 Hz for case 1. The low-frequency peaks as seen in the power spectrum of $u$ component and the 50 Hz peak, as seen in the power spectrum of $v$ velocity component in Figs. 11(a) and 11(c), are due to the vertical oscillation of the shear layer and the vortex shedding, respectively. For case 1, the vortex-shedding frequency is still visible in the power spectrum of $u$ fluctuating velocity component [see Fig. 11(a)], but its amplitude is less due to the coexistence of the low-frequency oscillation. Since the low-frequency oscillation is dominant in the case of the high adverse pressure gradient (case 2), there is no sign of vortex-shedding frequency in the power spectrum of the $u$ fluctuating

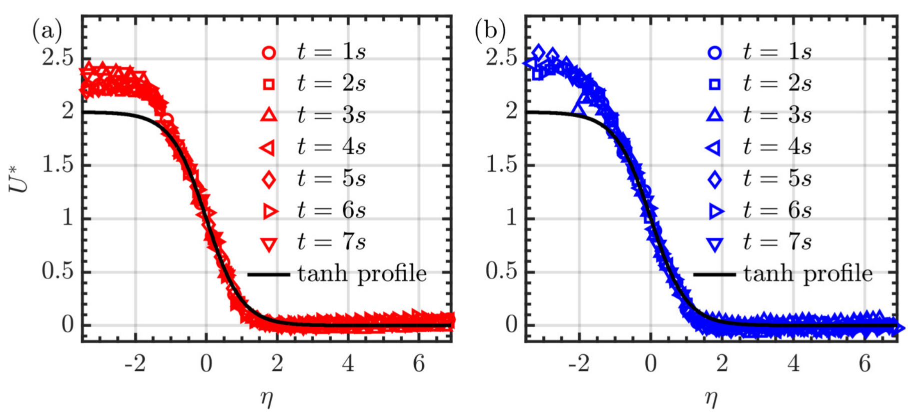


FIG. 10. Embedded shear layer scaling for the velocity profiles shown in Fig. 9. (a) Case 1. (b) Case 2.

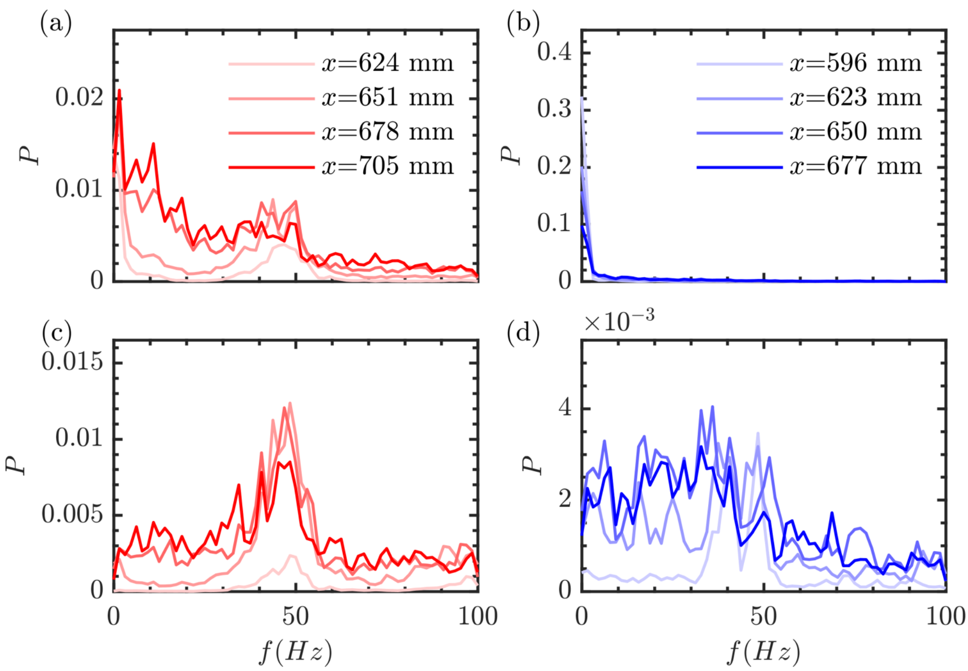


FIG. 11. Power spectra for the time series signals shown in Fig. 8. (a) and (b) Spectra for $u$ signals for case 1 and case 2, respectively. (c) and (d) Spectra for $v$ signals for case 1 and case 2, respectively. Power, $P$, is in arbitrary scale.

component [see Fig. 11(b)]. Since the low-frequency oscillation with high amplitude is present in the $u$ signal for case 2, its power spectrum is unable to produce the shedding frequency. Therefore, it may be misleading to conclude whether the vortex shedding is present or not in a flow, solely based on the power spectrum analysis of $u$ fluctuation. It actually depends on the relative amplitude of the low- and high-frequency oscillation present in the signal. If the amplitude of the low-frequency oscillation is less as compared to the one with high-frequency oscillation, then it is possible to get the vortex-shedding frequency using the power spectrum analysis of the $u$ component. However, the $v$ fluctuating velocity provides the vortex-shedding frequency information irrespective of their relative amplitudes.

Further, in the case of a low adverse pressure gradient (case 1), a dominant peak at about 50 Hz is seen at different downstream locations, whereas multiple peaks are seen to appear with downstream distance for the case of a high adverse pressure gradient (case 2). This is because of the fact that whenever the shear layer changes its instability characteristics (particularly, the location of the inflection point), it sheds vortices at different frequencies. Hence, one can see multiple frequency peaks with increasing streamwise distances [see Fig. 11(d)]. These several scales are due to the different coherent vortex structure formation as transition point changes with time. In order to investigate the different coherent vortex structures, proper orthogonal decomposition (POD) analysis has been carried out to decompose the actual flow field into several modes.

### C. POD analysis

Proper orthogonal decomposition (POD) is a widely used modal decomposition technique in fluid mechanics. It provides information about the coherent structure present in the complex flow

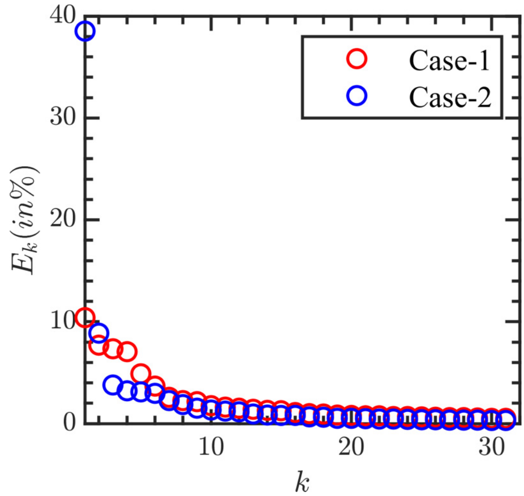


FIG. 12. Comparison of the relative energy levels between case 1 and case 2.

field. Using this analysis, the fluctuating flow field is decomposed in the following form,

$$\mathbf{v}'(\mathbf{x}, t_n) = \sum_k a^k(t_n)\Phi^k(\mathbf{x}), \tag{1}$$

where $\mathbf{v}'(\mathbf{x}, t_n)$ is the fluctuating flow field; $\Phi^k(\mathbf{x})$ and $a^k(t_n)$ are $k^{th}$ spatial POD mode shape and its time coefficient, respectively. Here, the fluctuating flow field consists of $u$ and $v$ components. The POD mode shapes and their time coefficients are estimated using the method of snapshot [64]. The POD methodology, as detailed in previous work [50], is briefly outlined here. The $u$ and $v$ fluctuating velocity components are arranged in a matrix, $A$. Autocovariance matrix, $C(= A^T A)$, is determined for the matrix $A$. The eigenvalues ($\lambda_k$) and their corresponding eigenvectors ($\phi^k$) are determined from the autocovariance matrix, $C$. The eigenvectors are arranged based on their energy level (eigenvalues). The eigenmodes/POD modes ($\Phi^k$) are determined using the relation

$$\Phi^k = \sum_{i=1}^{M} \phi_i{}^k \mathbf{v}'{}_i, \tag{2}$$

where $M$ is the number of snapshots/PIV realizations. The time coefficient ($a^k$) of the POD modes are calculated by the inner product of normalized $\Phi^k$ and $\mathbf{v}'$

$$a^k = (\mathbf{v}', \Phi^k). \tag{3}$$

The relative energy ($E_k$) of the POD modes is calculated by

$$E_k = \frac{\lambda_k}{\sum_{k=1}^{M} \lambda_k} \times 100\%. \tag{4}$$

The relative energy level ($E_k$) of each POD mode is shown in Fig. 12, for both the cases considered here. One can notice that the first four modes, for the low adverse pressure gradient (case 1), cover nearly 6–10 % of the relative energy. Moreover, the first mode is not coupled with the second mode as the energy levels are not the same in both cases. A similar observation has also been reported in the literature [65,66]. These authors concluded that those modes are not associated with the convective phenomenon of the separated shear layer, and it is due to the shear layer flapping. In fact, for the high adverse pressure gradient case (case 2), the first mode energy increases abruptly, as shown in Fig. 12. This increase in the energy is attributed to the increase in the amplitude of the

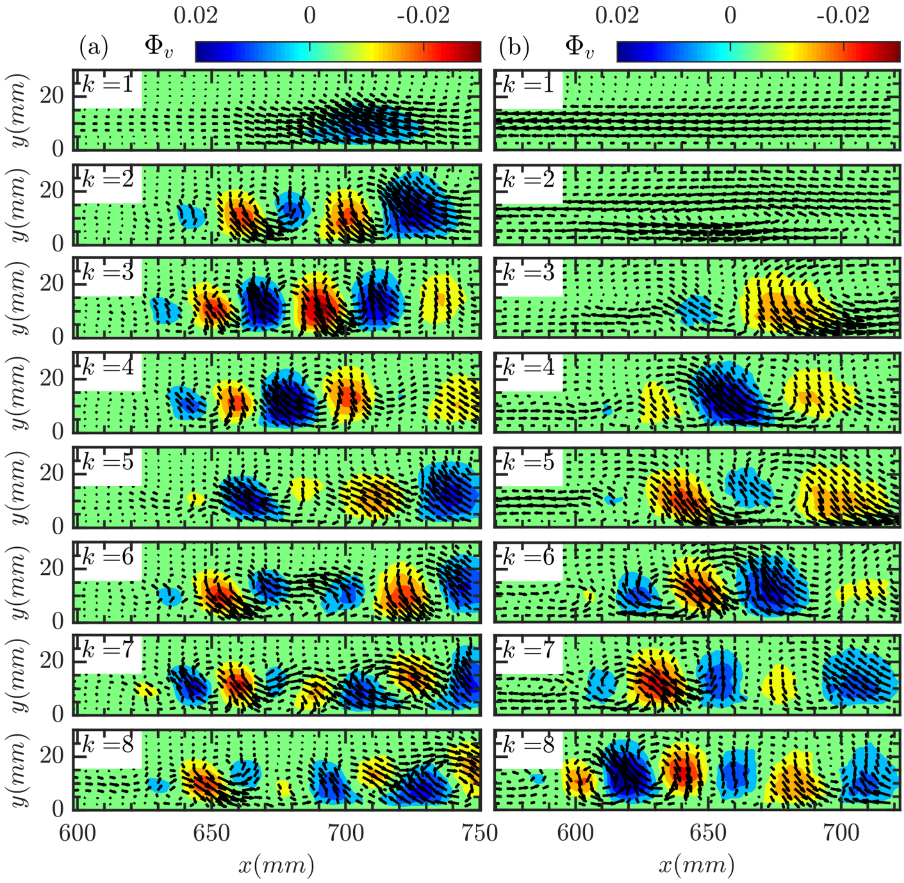


FIG. 13. POD mode shapes superimposed with the contours of its $v$ component. (a) Mode shapes for case 1 (low adverse pressure gradient case). (b) Mode shapes for case 2 (high adverse pressure gradient case).

low-frequency oscillation of the shear layer, as discussed earlier. Some dominant POD modes based on their relative energy levels are shown in Fig. 13. The first mode for case 1 is not correlated with any other lower-order modes. Similarly, the first two modes do not correlate with other lower-order modes for case 2, similar to those reported in the literature [43,66–68]. However, in those studies, the relative energy level of the first POD mode was nearly 10%, which is similar to the first mode for case 1 in the present study. Hence, the shear layer oscillation may not be significant in those studies except for the work reported by Michelis *et al.* [66], who did not investigate the higher-order modes. Typically, the vortex-shedding structures are identified by the presence of successive positive and negative $v$ fluctuating velocity components. The POD analysis of only $v$ fluctuating velocity component clearly supports this assertion, as discussed in the Appendix. But, the POD analysis based on both $u$ and $v$ fluctuating velocity components reveals the flow structures related to both the low- and high-frequency oscillations. Power spectra of the time coefficients ($a^k$) of the first eight POD modes in Fig. 14 clearly show that the first mode for case 1, and the first and the second modes for case 2 are associated with the low-frequency structure of the flow, whereas other higher-order modes are associated with higher frequencies. For example, a peak at about 50 Hz for case 1 can consistently be observed for $k = 2$–8, while the peaks for case 2 are seen to be different for different higher-order modes, which can be attributed to the movement of the inflectional point in the velocity profile as shown in Fig. 9. Therefore, the second- and the higher-order POD modes, as seen in Fig. 13(a), are involved with vortex shedding, for case 1. Similarly, the third- and the

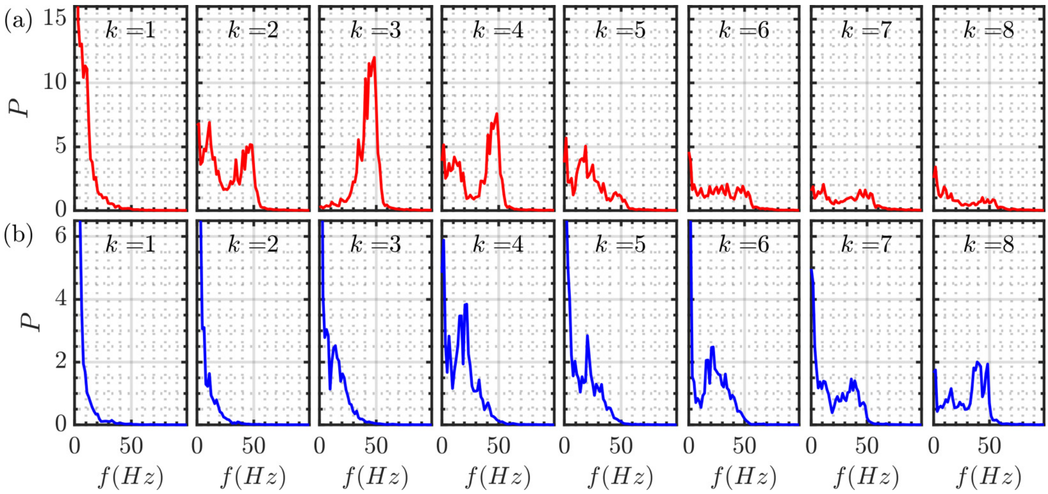


FIG. 14. Power spectra of the time coefficients of the POD modes. (a) Case 1. (b) Case 2.

higher-order POD modes, as seen in Fig. 13(b), are involved with vortex shedding, for case 2. Appearance of the shedding structure from the third mode onward, as seen in Fig. 13(b), is because of the fact that the high adverse pressure gradient for case 2 causes a significant low-frequency oscillation, as compared to case 1. One can also see in Fig. 13(b) that the location of the onset of the shedding mode shifts in the upstream direction as the mode number increases. This reaffirms the fact that the streamwise location where the flow undergoes transition shifts upstream. While the transition point moves upstream, it leads to an earlier vortex-shedding structure, as shown in Fig. 13(b). Such movement of the onset of vortex shedding is not clear in Fig. 13(a), mainly due to the small amplitude of the low-frequency oscillation.

It is often reported in the literature [43,66] that the first dominant mode is perhaps associated with low-frequency oscillation of the separated shear layer, albeit without any proper evidence. The present time-resolved measurements allow us to calculate the time series of the POD coefficients. The time coefficient of the first POD mode is compared with the instantaneous $\delta_I^*$, as shown in Fig. 15. In both cases, the shear layer oscillations resemble the time series of the POD coefficient. In fact, it is better seen in Fig. 15(b), for case 2. Hence, the present POD analysis of the time-resolved data clearly confirms the speculation that the first POD mode is associated with the low-frequency oscillation of the shear layer.

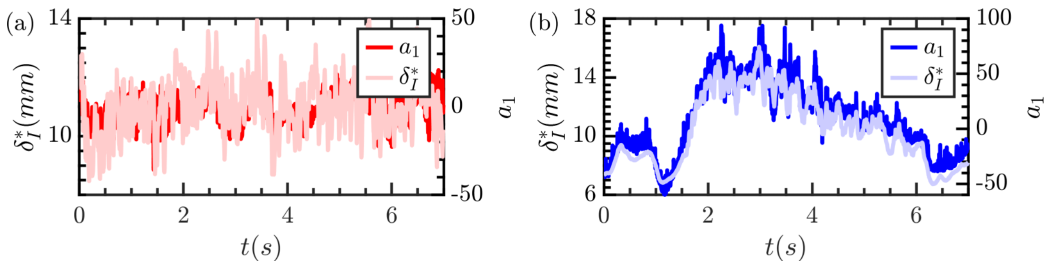


FIG. 15. Comparison of the instantaneous displacement thickness with the time coefficient of first POD mode. (a) Comparison for case 1 (low adverse pressure gradient case). (b) Comparison for case 2 (high adverse pressure gradient case).

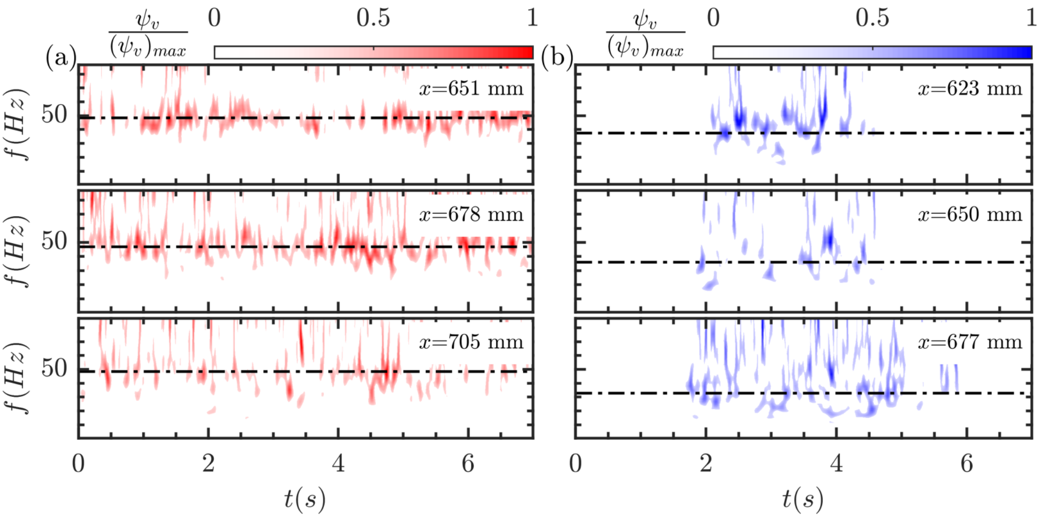


FIG. 16. Contours of the normalized wavelet coefficients for the $v$ time-series signal at different streamwise locations. A dashed line shows the peak frequency obtained from the power spectra of the same signal.

From these above observations, we propose that $\delta^*_{\mathrm{rms}}$ is an important parameter in a separated shear layer to characterize the intensity of a low-frequency oscillation. The estimated values of $\delta^*_{\mathrm{rms}}$ for the present study are found to be 0.54 and 2.47, for case 1 and case 2, respectively. The nondimensional values ($\delta^*_{\mathrm{rms}}/\delta^*$) are found to be 0.05 and 0.23, for case 1 and case 2, respectively; note that $\delta^*$ is estimated from the mean velocity profile. It implies, when $\delta^*_{\mathrm{rms}}/\delta^* \to 0$, the instability of a separated flow will occur solely via convective amplification. On the other hand, if $\delta^*_{\mathrm{rms}}/\delta^*$ has a finite value, then there will be an interaction of the vertical oscillation of the separated shear layer and the convective instability of the separated shear layer. The value of $\delta^*_{\mathrm{rms}}$ in the present study indicates that a low-frequency oscillation exists even in the low adverse pressure gradient case (case 1), as well. In fact, the first POD mode also shows the low-frequency oscillation for case 1.

The wavelet analysis of time series is often carried out for localization of frequency in time [69]. Therefore, the intermittent nature of the vortex-shedding frequency can be identified by the wavelet analysis. The wavelet analysis has been carried out for the time-series signal shown in last three panels in Fig. 8. Since the $v$ component is suitable for the vortex-shedding signal, continuous wavelet transform is carried out for the $v$ component signal. The absolute value of the wavelet coefficient is estimated using the Morlet wavelet and is normalized by its maximum value for better visualization, as reported in the literature [70]. The wavelet contours, for the case 1 and case 2, are shown in Figs. 16(a) and 16(b), respectively. One can clearly see in Fig. 16(a) the signature of regular vortex shedding at about 50 Hz from $x = 651$ mm onward, for case 1, as the values of the wavelet coefficient are uniformly distributed about 50 Hz frequency along the time axis. On the other hand, Fig. 16(b) shows that the vortex shedding is intermittent, as the contours of the wavelet coefficients are localized in time and frequency axis, for case 2. One can also see that the time duration and the spread in the frequency axis of the wavelet contours are increasing in the downstream direction. This indicates that the number of scales increases in the downstream direction due to the movement of the transition point. Vortex shedding in the interval of $0 \leqslant t \leqslant 1.6$ s and $t \geqslant 6$ s in Fig. 16(b) is not present as the contour values of the wavelet coefficient are negligible. This is consistent with the vorticity contour, as shown in Fig. 6.

The above analyses confirm the presence of the low-frequency oscillation and its effect on vortex shedding. However, how this low-frequency or vertical oscillation originates in the separated shear layer is unclear. To shed some light on this, we investigated the temporal behavior of the reverse

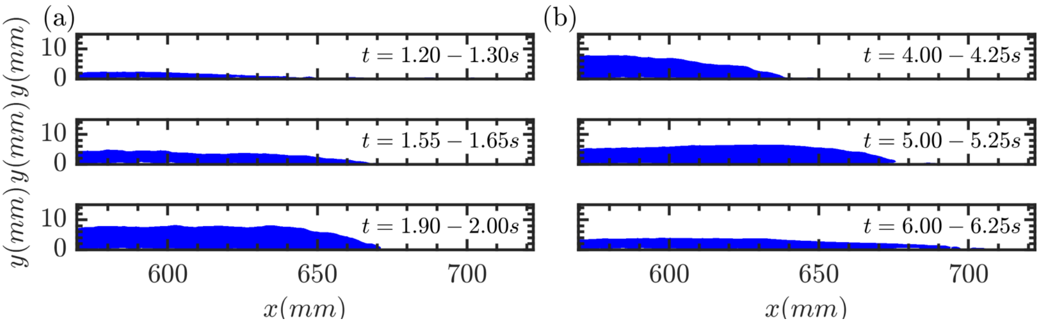


FIG. 17. Time evolution of the reverse flow contours estimated from the short time average of instantaneous streamwise velocity for case 2. (a) Non-vortex-shedding state to vortex-shedding state. (b) Vortex-shedding to non-vortex-shedding state.

flow region to get the underlying mechanism for the low-frequency oscillation of the separated shear layer. We considered case 2 since its low-frequency amplitude is high. Instead of inspecting the reverse flow region at a particular time instant, a short time average of the instantaneous streamwise velocity at all the locations has been carried out simultaneously and plotted as contours of the short time-averaged data in the $x$-$y$ plane, as shown in Fig. 17. It is to be noted here that we plotted only the reverse flow contours for better understanding in this figure. As seen in Figs. 6 and 7 ($t \approx$ 1–2 s), the flow quickly changes to shedding state from a nonshedding state. Within this time period, Fig. 17(a) also shows that the reverse flow region gets amplified in the vertical direction, leading to outward movement of the shear layer and vortex shedding due to the onset of instability. On the other hand, Fig. 17(b) shows that the reverse flow region extends in the streamwise direction with time. It is because the shed vortices carry low-momentum fluid in the downstream direction, leading to inward (or towards the wall) movement of the shear layer. Consequently, the viscous effect dampens the inflectional instability, and the transition point is moved in the downstream direction, as discussed earlier. Further extension of reverse flow region downstream, the reverse flow region becomes thinner in the vertical direction, resulting in a stable shear layer/nonshedding shear layer. The summary of the transition mechanism under a high-adverse pressure gradient is shown in Fig. 18.

### D. Time series signals of the fluctuating velocity for the longer duration

A question may arise whether the above transition mechanism is valid even for a longer time or not. Due to the memory limitation of the continuous data acquisition for a longer period of time using a TR-PIV system, we carried out continuous measurements at various $x$ and $y$ locations for a longer period of time using the hot-wire anemometry technique. The mean velocity profiles of the hot-wire measurements were found to compare well with those obtained from the PIV measurements (not shown here for brevity). The fluctuating velocity ($u = U_I - U$) signals at various $x$ locations are shown in Figs. 19(a) and 19(b), for cases 1 and 2, respectively. It should be noted that these data are measured approximately at the wall-normal location where the value of $u_{\mathrm{rms}}$ is found to be maximum. For better visualization, the fluctuating signal, for just a period of 10 s, as marked by a rectangle, is zoomed in, and shown in the inset of each panel of Fig. 19. The low-frequency oscillation is clearly visible at $x = 624$ mm and $x = 590$ mm, for case 1 and case 2, respectively. Further downstream, the high-frequency oscillation is significant in the fluctuating velocity signal for case 1, which is found to be more regular. On the other hand, the high-frequency oscillation is found to be intermittent for case 2. This can clearly be seen in the zoomed-in view of the fluctuating velocity signal. Similar intermittent high-frequency oscillation is also observed by Gaster [22] for the case of a long bubble.

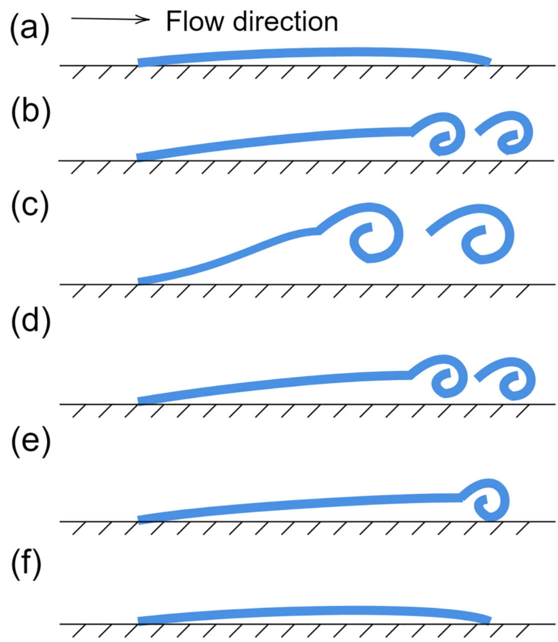


FIG. 18. Schematic of the transition mechanism of the separated shear layer under the high level of adverse pressure gradient, i.e., for case 2.

Further, histograms of the $u$ signals in Fig. 19 are shown in Figs. 20(a) and 20(b), for both case 1 and case 2, respectively. The histogram for case 1 in Fig. 20(a) shows a bell-shaped distribution. This is due to the regular oscillation of the $u$ signal about $u = 0$, which confirms the regular vortex shedding. On the other hand, case 2 shows a left-skewed distribution [Fig. 20(b)]. The left skewness is due to a stable shear layer, as $u$ sometimes remains almost constant for a considerable length of time, as shown in the inset of the Fig. 19(b). This constant value without any significant oscillation leads to the peak probability values in the histogram, as shown in Fig. 20(b). Consequently, the histogram distribution becomes a left-skewed one. This analysis thus suggests that the left-skewed distribution of the histogram is an indicator of the intermittent vortex shedding in a separated shear layer.

## IV. CONCLUSION

A contoured wall is used to impose an adverse pressure gradient in a flow over a flat plate. Using two different contoured walls, two different levels of adverse gradients were imposed in the flow. To study the unsteady characteristics of the separated shear layer, we carried out TR-PIV measurements with high spatial resolutions in the transitional region of a separated shear layer.

In the case of a low adverse pressure gradient, the separated shear layer was found to be associated with regular vortex shedding for the entire duration of the measurements. The low-frequency oscillation of the separated shear layer in this case is not significant. In contrast, the low-frequency oscillation associated with the separated shear layer for the high adverse pressure gradient case is significantly high. This affects the regular shedding characteristics of the separated shear layer. Due to this low-frequency oscillation and the associated movement of the points of inflection in the velocity profiles [Fig. 9(b)], vortex shedding is found to be intermittent for the high adverse pressure gradient case. It takes the separated shear layer from a vortex-shedding state to a non-vortex-shedding state and vice versa. The reverse flow region was found to am-

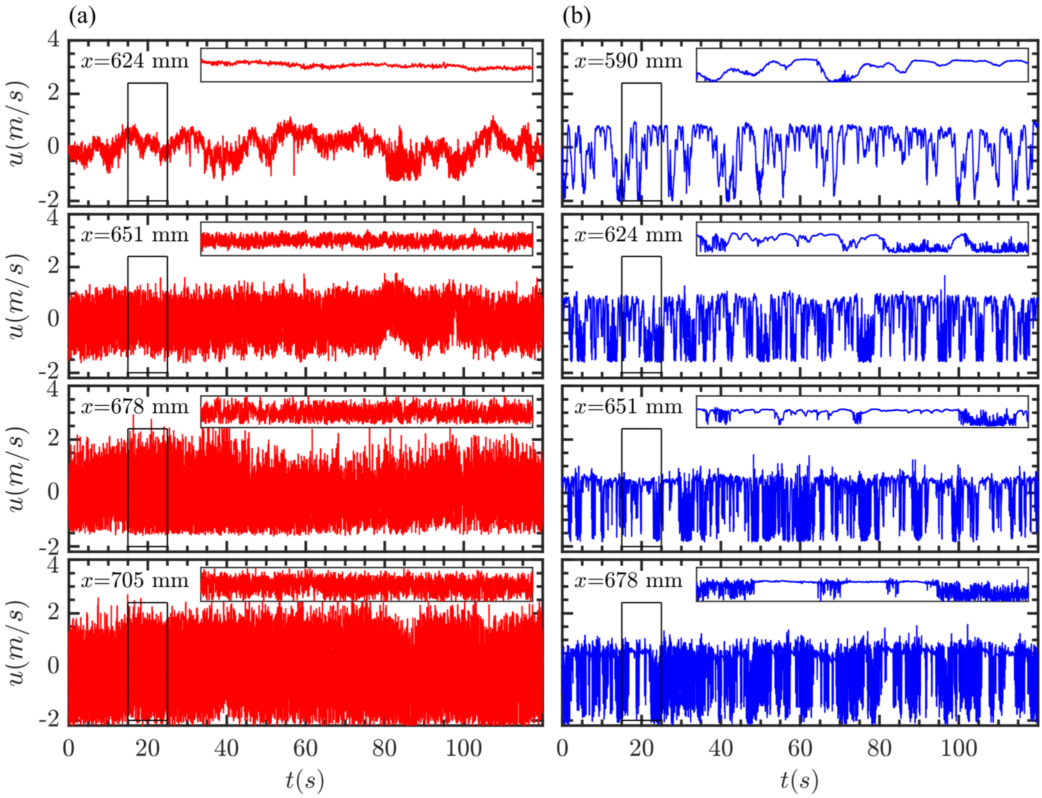


FIG. 19. Comparison of the fluctuating velocity signals (obtained using the hot-wire anemometry technique) for (a) case 1 and (b) case 2. Inset in each panel shows a zoomed-in view of the time-series signal marked by a rectangle.

plify with time when the shear layer is in nonshedding state. When the reverse flow region is amplifying, the shear layer is vertically moved outward, and it then becomes prone to inflectional instability. Consequently, vortex shedding/transition starts in the separated shear layer. Due to these vortices, low-momentum fluid is pumped upward and gets carried away in the downstream. As a result, the reverse flow region shrinks in the vertical direction and extends in the downstream direction with time. This eventually enhances the stability of the separated shear layer, leading to suppression of vortex shedding. This is attributed to the existence of the low-frequency oscillation of the shear layer. In the process of intermittent vortex shedding, the short time-averaged velocity profiles near the onset of $v_{\mathrm{rms,max}}$ growth follow the embedded shear layer scaling [1]. The histogram of $u$ shows the left-skewed distribution for the case of intermittent vortex shedding (case 2), whereas it shows a bell-shaped distribution for the regular vortex shedding case (case 1).

However, based on the investigation, we propose a parameter $\delta^*_{\mathrm{rms}}/\delta^*$, which determines the interaction level of the low-frequency oscillation on high-frequency vortex shedding/oscillation of the separated shear layer. To the best of our knowledge, this parameter has not been discussed or reported in the earlier separated shear layer studies. It indicates that the effect of low-frequency oscillation on high-frequency vortex shedding vanishes when $\delta^*_{\mathrm{rms}}/\delta^* \to 0$. Further, it is found that the separated shear layer changes its vortex-shedding state to non-vortex-shedding state, and vice versa when $\delta^*_{\mathrm{rms}}/\delta^* \to 0.23$.

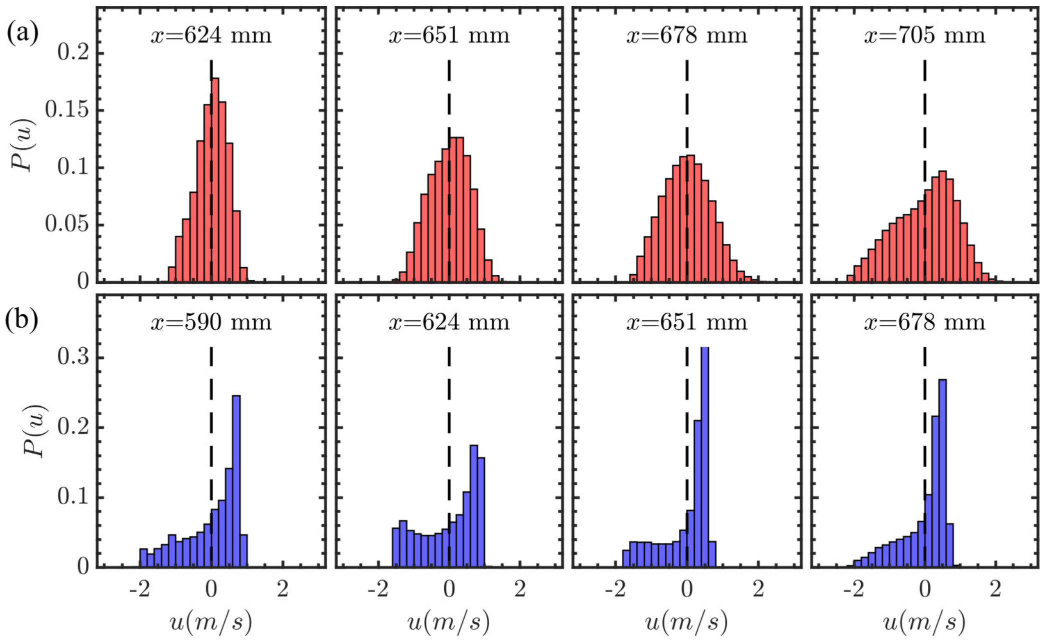


FIG. 20. Histogram for the fluctuating velocity signals (obtained using the hot-wire anemometry technique. (a) Case 1. (b) Case 2.

## ACKNOWLEDGMENTS

The authors gratefully acknowledge the financial support received from Indian Institute of Technology, Kanpur, and from SERB, DST (EMR/2015/001042). We sincerely thank Prof. V. Shankar and Prof. K. Poddar for sharing their CMOS cameras to carry forward this work. We also sincerely thank Dr. Shyam Sunder Gopalakrishnan for his valuable comments and suggestions on

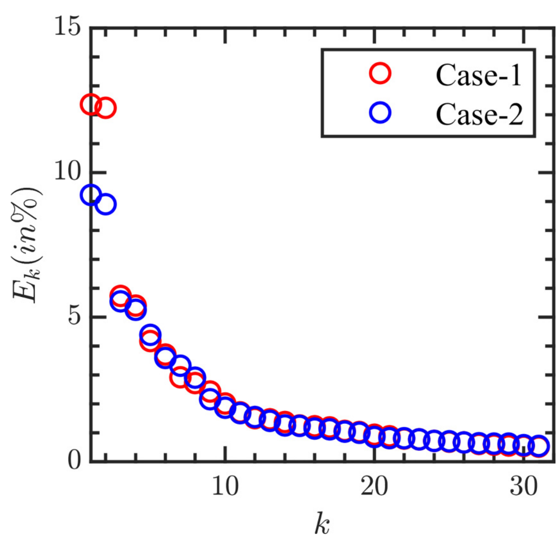


FIG. 21. Comparison of the v-POD relative energy levels between case 1 and case 2.

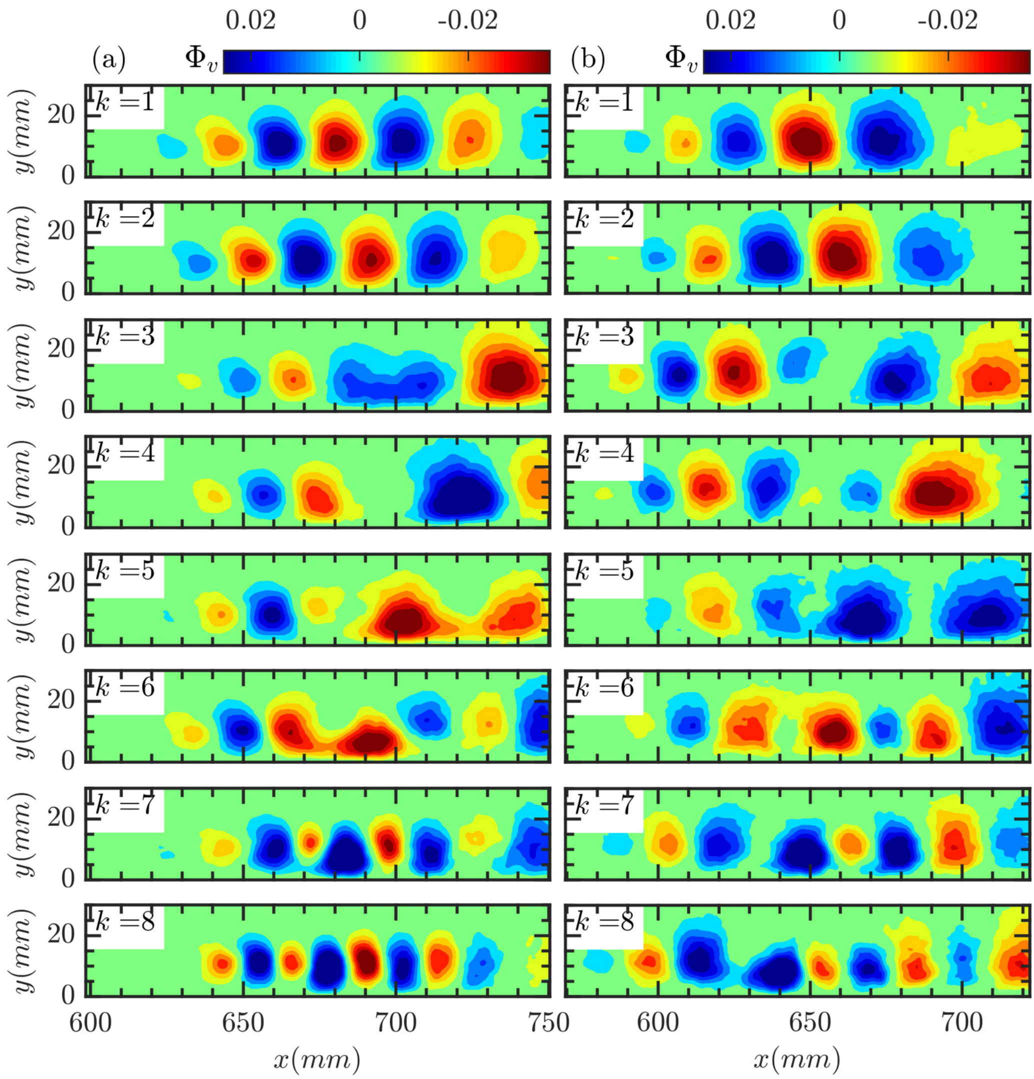


FIG. 22. v-POD mode shapes. (a) Mode shapes for case 1 (low adverse pressure gradient case). (b) Mode shapes for case 2 (high adverse pressure gradient case).

this manuscript. We would also like to thank the members of the low-speed aerodynamics laboratory for their assistance in performing the experiments.

## APPENDIX

The present data reveal that the $v$ fluctuating velocity was not affected by the low-frequency oscillation (Fig. 8). Therefore, the POD analysis of only the $v$ fluctuating velocity, which is referred as $v$-POD analysis, is expected to reveal the shedding characteristics for both cases. In addition, the POD analysis provides the global characteristics of a flow, which are different from the local characteristics obtained from a velocity time series. For the $v$-POD analysis, we follow the same procedure that was also used for the $uv$-POD analysis to calculate the relative energy level ($E_k$), mode shapes ($\phi_v$) and the power spectra of the POD time coefficients. Figure 21 clearly shows that the most energetic modes are coupled, that is, two modes have nearly the same energy level. This

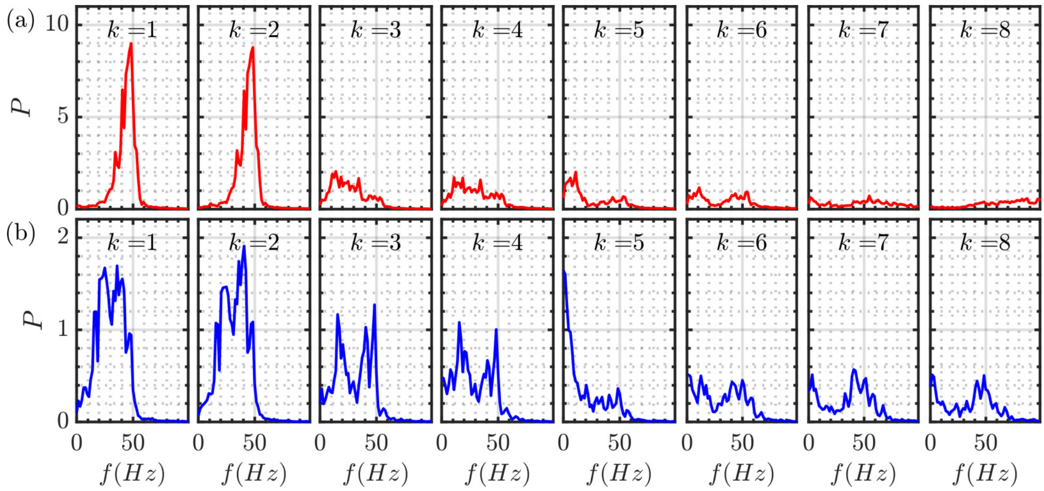


FIG. 23. Power spectra of the time-coefficients of the POD modes. (a) Case 1, (b) Case 2.

indicates the presence of a convective structure in the flow for both the cases, e.g., Refs. [7,50,61]. Moreover, one can see that the value of $E_k$ is higher for case 1, indicating the fact that there exists a regular vortex shedding for case 1, as compared to case 2. The decrease in energy in case 2 indicates variations/reduction in the coherent pattern of the vortex shedding process, which is actually due to the intermittent vortex shedding. However, the POD mode shapes associated with the first eight dominant modes are shown in Figs. 22(a) and 22(b) for case 1 and case 2, respectively. The first two mode shapes show a spatial shift with alternate positive and negative fluctuations, which confirm the presence of vortex shedding. In fact, the power spectra of the $v$-POD time coefficients corresponding to the mode shapes shown in Fig. 22 are presented in Figs. 23(a) and 23(b), for case 1 and case 2, respectively. One can notice that the coupled modes have the same frequency contents in both cases, as expected. Comparing the power spectra of the first two modes for both cases, one can find the broadened power spectra for case 2, as compared to case 1. This can be attributed to the vertical movement of the inflection point, which leads to different coherent structures with different frequencies.

[1] D. M. Schatzman and F. O. Thomas, An experimental investigation of an unsteady adverse pressure gradient turbulent boundary layer: embedded shear layer scaling, J. Fluid Mech. **815**, 592 (2017).

[2] S. Gudmundsson, *General Aviation Aircraft Design: Applied Methods and Procedures* (Butterworth-Heinemann, London, 2013).

[3] G. P. Corten, Flow separation on wind turbine blades, Ph.D. thesis, Utrecht University, 2001.

[4] L. Landweber and V. C. Patel, Ship boundary layers, Annu. Rev. Fluid Mech. **11**, 173 (1979).

[5] S. R. Ahmed, G. Ramm, and G. Faltin, Some salient features of the time-averaged ground vehicle wake, SAE Transactions **93**, 473 (1984).

[6] Z. Yang, On bypass transition in separation bubbles: A review, Propul. Power Res. **8**, 23 (2019).

[7] S. Hosseinverdi and H. F. Fasel, Role of klebanoff modes in active flow control of separation: Direct numerical simulations, J. Fluid Mech. **850**, 954 (2018).

[8] A. V. Dovgal, V. V. Kozlov, and A. Michalke, Laminar boundary layer separation: instability and associated phenomena, Prog. Aeronaut. Sci. **30**, 61 (1994).

[9] S. S. Diwan and O. N. Ramesh, On the origin of the inflectional instability of a laminar separation bubble, J. Fluid Mech. **629**, 263 (2009).

[10] J. H. Watmuff, Evolution of a wave packet into vortex loops in a laminar separation bubble, J. Fluid Mech. **397**, 119 (1999).

[11] O. Marxen, M. Lang, and U. Rist, Vortex formation and vortex breakup in a laminar separation bubble, J. Fluid Mech. **728**, 58 (2013).

[12] L. E. Jones, R. D. Sandberg, and N. D. Sandham, Direct numerical simulations of forced and unforced separation bubbles on an airfoil at incidence, J. Fluid Mech. **602**, 175 (2008).

[13] J. H. Almutairi and I. M. AlQadi, Large-eddy simulation of natural low-frequency oscillations of separating–reattaching flow near stall conditions, AIAA J. **51**, 981 (2013).

[14] K. B. M. Q. Zaman, D. J. McKinzie, and C. L. Rumsey, A natural low-frequency oscillation of the flow over an airfoil near1 stalling conditions, J. Fluid Mech. **202**, 403 (1989).

[15] M. B. Bragg, D. C. Heinrich, and A. Khodadoust, Low-frequency flow oscillation over airfoils near stall, AIAA J. **31**, 1341 (1993).

[16] M. B. Bragg, D. C. Heinrich, F. A. Balow, and K. B. M. Q. Zaman, Flow oscillation over an airfoil near stall, AIAA J. **34**, 199 (1996).

[17] A. P. Broeren and M. B. Braggt, Unsteady stalling characteristics of thin airfoils at low Reynolds number, *Fixed and Flapping Wing Aerodynamics for Micro Air Vehicle Applications* (American Institute of Aeronautics, Reston, 2001), p. 191.

[18] J. AlMutairi, E. ElJack, and I. AlQadi, Dynamics of laminar separation bubble over naca-0012 airfoil near stall conditions, Aero. Sci. Tech. **68**, 193 (2017).

[19] N. Alferez, I. Mary, and E. Lamballais, Study of stall development around an airfoil by means of high fidelity large eddy simulation, Flow, Turbul. Combust. **91**, 623 (2013).

[20] E. M. Eljack and J. Soria, Investigation of the low-frequency oscillations in the flowfield about an airfoil, AIAA J. **58**, 4271 (2020).

[21] E. Eljack, J. Soria, Y. Elawad, and T. Ohtake, Simulation and characterization of the laminar separation bubble over a naca-0012 airfoil as a function of angle of attack, Phys. Rev. Fluids **6**, 034701 (2021).

[22] M. Gaster, The structure and behaviour of laminar separation bubbles, Technical Report, 1967.

[23] P. R. Owen and L. Klanfer, On the laminar boundary layer separation from the leading edge of a thin aerofoilv, Technical Report, Aeronautical Research Council London, 1953.

[24] S. S. Diwan, S. J. Chetan, and O. N. Ramesh, On the bursting criterion for laminar separation bubbles, in *IUTAM Symposium on Laminar-Turbulent Transition* (Springer, Berlin, 2006), pp. 401–407.

[25] L. F. Crabtree, *The Formation of Regions of Separated Flow on Wing Surfaces* (HM Stationery Office, London, 1959).

[26] A. Mitra and O. N. Ramesh, New correlation for the prediction of bursting of a laminar separation bubble, AIAA J. **57**, 1400 (2019).

[27] D. E. Gault, Boundary-layer and stalling characteristics of the NACA 63-009 airfoil section, Technical Note No. 1894, National Advisory Committee for Aeronautics (1949).

[28] G. B. McCullough and D. E. Gault, Examples of three representative types of airfoil section stall at low speeds, NACA TN No. 2502 (1951).

[29] J. H. Almutairi, L. E. Jones, and N. D. Sandham, Intermittent bursting of a laminar separation bubble on an airfoil, AIAA J. **48**, 414 (2010).

[30] M. Alam and N. D. Sandham, Direct numerical simulation of ‘short’laminar separation bubbles with turbulent reattachment, J. Fluid Mech. **410**, 1 (2000).

[31] M. Kiya and K. Sasaki, Structure of a turbulent separation bubble, J. Fluid Mech. **137**, 83 (1983).

[32] N. J. Cherry, R. Hillier, and M. E. M. P. Latour, Unsteady measurements in a separated and reattaching flow, J. Fluid Mech. **144**, 13 (1984).

[33] M. Kiya and K. Sasaki, Structure of large-scale vortices and unsteady reverse flow in the reattaching zone of a turbulent separation bubble, J. Fluid Mech. **154**, 463 (1985).

[34] N. J. Cherry, R. Hillier, and M. E. M. P. Latour, The unsteady structure of two-dimensional separated-and-reattaching flows, J. Wind Engin. Ind. Aero. **11**, 95 (1983).

[35] I. P. Castro and A. Haque, The structure of a shear layer bounding a separation region. part 2. effects of free-stream turbulence, J. Fluid Mech. **192**, 577 (1988).

[36] Z. Yang and I. E. Abdalla, Effects of free-stream turbulence on large-scale coherent structures of separated boundary layer transition, Int. J. Numer. Meth. Fluids **49**, 331 (2005).
[37] Z. Yang and I. E. Abdalla, Effects of free-stream turbulence on a transitional separated–reattached flow over a flat plate with a sharp leading edge, Int. J. Heat Fluid Flow **30**, 1026 (2009).
[38] D. M. Driver, H. L. Seegmiller, and J. G. Marvin, Time-dependent behavior of a reattaching shear layer, AIAA J. **25**, 914 (1987).
[39] J. K. Eaton and J. P. Johnston, Low frequency unsteadyness of a reattaching turbulent shear layer, in *Turbulent Shear Flows 3* (Springer, Berlin, 1982), pp. 162–170.
[40] P. G. Spazzini, G. Iuso, M. Onorato, N. Zurlo, and G. M. Di Cicca, Unsteady behavior of back-facing step flow, Exp. Fluids **30**, 551 (2001).
[41] G. Balamurugan and A. C. Mandal, Experiments on localized secondary instability in bypass boundary layer transition, J. Fluid Mech. **817**, 217 (2017).
[42] G. Balamurugan, A. Rodda, J. Philip, and A. C. Mandal, Characteristics of the turbulent non-turbulent interface in a spatially evolving turbulent mixing layer, J. Fluid Mech. **894**, A4(2020).
[43] D. Simoni, D. Lengani, M. Ubaldi, P. Zunino, and M. Dellacasagrande, Inspection of the dynamic properties of laminar separation bubbles: free-stream turbulence intensity effects for different reynolds numbers, Exp. Fluids **58**, 66 (2017).
[44] R. E. Hanson, H. P. Buckley, and P. Lavoie, Aerodynamic optimization of the flat-plate leading edge for experimental studies of laminar and transitional boundary layers, Exp. Fluids **53**, 863 (2012).
[45] Y. Li and M. Gaster, Active control of boundary-layer instabilities, J. Fluid Mech. **550**, 185 (2006).
[46] J. P. Holman, *Experimental Methods for Engineers*, Vol s1–VIII. 8th ed (McGRaw Hill, New York, 2011).
[47] M. Raffel, C. E. Willert, F. Scarano, C. J. Kähler, S. T. Wereley, and J. Kompenhans, *Particle Image Velocimetry: A Practical Guide* (Springer, Berlin, 2018).
[48] W. Thielicke, The flapping flight of birds: Analysis and application, Ph.D. thesis, University of Groningen, 2014.
[49] L. Gui and S. T. Wereley, A correlation-based continuous window-shift technique to reduce the peak-locking effect in digital piv image evaluation, Exp. Fluids **32**, 506 (2002).
[50] A. C. Mandal, L. Venkatakrishnan, and J. Dey, A study on boundary-layer transition induced by free-stream turbulence, J. Fluid Mech. **660**, 114 (2010).
[51] E. J. Fitzgerald and T. J. Mueller, Measurements in a separation bubble on a airfoil using laser velocimetry, AIAA J. **28**, 584 (1990).
[52] C. Haggmark, Investigations of disturbances developing in a laminar separation bubble flow, Ph.D. thesis, Royal Institute of Technology, Stockholm, 1987.
[53] C. P. Häggmark, A. A. Bakchinov, and P. H. Alfredsson, Experiments on a two–dimensional laminar separation bubble, Philos. Trans. R. Soc. London A **358**, 3193 (2000).
[54] H. J. Li and Z. Yang, Separated boundary layer transition under pressure gradient in the presence of free-stream turbulence, Phys. Fluids **31**, 104106 (2019).
[55] J. D. Coull and H. P. Hodson, Unsteady boundary-layer transition in low-pressure turbines, J. Fluid Mech. **681**, 370 (2011).
[56] R. H. Ellsworth and T. J. Mueller, Airfoil boundary layer measurements at low re in an accelerating flow from a nonzero velocity, Exp. Fluids **11**, 368 (1991).
[57] J. W. Kurelek, M. Kotsonis, and S. Yarusevych, Transition in a separation bubble under tonal and broadband acoustic excitation, J. Fluid Mech. **853**, 1 (2018).
[58] T. M. Kirk and S. Yarusevych, Vortex shedding within laminar separation bubbles forming over an airfoil, Exp. Fluids **58**, 43 (2017).
[59] M. S. H. Boutilier and S. Yarusevych, Separated shear layer transition over an airfoil at a low reynolds number, Phys. Fluids **24**, 084105 (2012).
[60] W. Balzer and H. F. Fasel, Numerical investigation of the role of free-stream turbulence in boundary-layer separation, J. Fluid Mech. **801**, 289 (2016).
[61] S. Hosseinverdi and H. F. Fasel, Numerical investigation of laminar–turbulent transition in laminar separation bubbles: the effect of free-stream turbulence, J. Fluid Mech. **858**, 714 (2019).

[62] K. Anand and S. Sarkar, Features of a laminar separated boundary layer near the leading-edge of a model airfoil for different angles of attack: an experimental study, J. Fluids Eng. **139**, 021201(2017).

[63] M. Nishioka, M. Asai, and S. Yoshida, Control of flow separation by acoustic excitation, AIAA J. **28**, 1909 (1990).

[64] L. Sirovich, Turbulence and the dynamics of coherent structures. i. coherent structures, Q. Appl. Math. **45**, 561 (1987).

[65] D. Lengani, D. Simoni, M. Ubaldi, and P. Zunino, Pod analysis of the unsteady behavior of a laminar separation bubble, Exp. Therm. Fluid Sci. **58**, 70 (2014).

[66] T. Michelis, S. Yarusevych, and M. Kotsonis, Response of a laminar separation bubble to impulsive forcing, J. Fluid Mech. **820**, 633 (2017).

[67] A. Mohammed-Taifour and J. Weiss, Unsteadiness in a large turbulent separation bubble, J. Fluid Mech. **799**, 383 (2016).

[68] X. Ma and A. Schröder, Analysis of flapping motion of reattaching shear layer behind a two-dimensional backward-facing step, Phys. Fluids **29**, 115104 (2017).

[69] J. Lewalle, D. E. Ashpis, and K. H. Sohn, Demonstration of wavelet techniques in the spectral analysis of bypass transition data, NASA Technical Publication Report No. NASA-TP-3555 (1997).

[70] S. Pröbsting and S. Yarusevych, Laminar separation bubble development on an airfoil emitting tonal noise, J. Fluid Mech. **780**, 167 (2015).